MDPI

Article

Defective ZnO Nanoflowers Decorated by Ultra-Fine Pd Clusters for Low-Concentration CH_4 Sensing: Controllable Preparation and Sensing Mechanism Analysis

Yang Chen [1], Wenshuang Zhang [1], Na Luo [1], Wei Wang [2,*] and Jiaqiang Xu [1,*]

[1] NEST Lab, Department of Physics, Department of Chemistry, College of Sciences, Shanghai University, Shanghai 200444, China; cyshu@shu.edu.cn (Y.C.); wszhang21@m.fudan.edu.cn (W.Z.); nihaoluona@163.com (N.L.)

[2] NMPA Key Laboratory for Respiratory and Anaesthetic Equipment, Shanghai Institute of Medical Device Testing, Shanghai 200431, China

* Correspondence: 13916234940@163.com (W.W.); xujiaqiang@shu.edu.cn (J.X.); Tel.: +86-021-66132663 (J.X.)

Abstract: To detect low concentration of CH_4 is indeed meaningful in industrial manufacturing, such as the petrochemical industry and natural gas catalysis, but it is not easy to detect low concentration of CH_4 due to its high symmetrical and stable structure. In this work, defect-rich ZnO_{1-x} nanoflowers (NFs) were synthesized by a two-step route so as to obtain defect-enhanced gas-sensing performance, namely hydrothermal synthesis followed by H_2 treatment. In order to achieve low-concentration detection of CH_4, the ultra-thin Pd clusters' (Cs, diameter about 1–2 nm) sensitizer was synthesized and decorated onto the surface of ZnO_{1-x} NFs. It is found that Pd Cs-2/ZnO_{1-x} gas sensors show enhanced gas-sensing properties to CH_4, even at ppm concentration level. At its optimal working temperature of 260 °C, the gas response to 50 ppm CH_4 can reach 5.0 with good gas selectivity; the response and recovery time is only 16.2 and 13.8 s, respectively. In the Results, we discussed the CH_4 gas-sensing mechanism deeply. Overall, it is very necessary to detect low-concentration methane safely. It is possible for further safe detection of low-concentration methane gas in the future.

Keywords: CH_4 gas sensor; ZnO_{1-x} nanoflowers; oxygen defects; Pd clusters

1. Introduction

Methane (CH_4) is a kind of dangerous gas. If the concentration in the air was as high as 5% to 15%, it would cause a severe explosion accident, which poses a great threat to life. In addition, it is a powerful greenhouse gas and a major component of natural gas. It is also released from coal mines, landfills, biomass combustion, and intestinal fermentation of ruminants such as cattle, sheep, and pigs. In addition, it is also a significant biomarker of some diseases [1–3]. Therefore, the detection of CH_4 is very important. However, there are few studies on the detection of ultra-low-concentration CH_4, mainly due to its stable structure. However, it is indeed essential to develop gas sensors for detecting low-concentration CH_4, which is of great significance for industrial production, methane transportation, and household daily methane leakage detection.

One of the most popular candidates is metal oxide semiconductor (MOS) gas sensors, due to their high sensitivity, easiness to integrate, etc., such as SnO_2, ZnO, TiO_2, and WO_3 [4–6]. Compared with other sensing materials, many advantages of MOS could be found in gas sensors. Firstly, MOS has high chemical and thermal stability in the air atmosphere even at a temperature of several hundred degrees, meaning its working environment can be harsh, however, many other gas-sensing materials do not have such functions, such as MOFs sensing material. Besides, the MOS sensors are resistant to humidity even working at more than 100 °C, but some sensors, such as quartz crystal microbalance (QCM) working at room temperature, could not work stably under the influence of humidity. At least, MOS sensors are sensitive to

most gases, and their sensing performances could be tuned by element doping, noble metal decorating, compositing with other sensing materials, and a different exposed crystal face. Whereas graphene-based and molecularly imprinted polymer-based sensors are too delicate to do so [7–10]. Among them, ZnO is a classic n-type MOS gas-sensing material because it is easy to produce lattice defects and oxygen vacancy defects on the surface, resulting in a great gas-sensing performance [11,12]. Nevertheless, sensors based on pure ZnO cannot satisfy daily demands of real time and rapid detection of low concentration of CH_4 because of its high symmetry structure.

Noble metals, such as Pt, Pd, Au, and Rh, often exhibit some novel features and functions owing to their excellent catalysis effect, so they have a broad application in different fields, such as energy storage, energy conversion, and biomedical diagnosis [13,14]. Thus, it is meaningful to enhance ZnO gas-sensing performance by adding noble metals such as Pd, Au, Pt, etc. Among them, Pd is an important catalyst because it has distinctive catalytic properties and electron sensitization [15]. The ZnO nanowires decorated with Pd nanoparticles reported by Yuan Zhang et al. show a much better response to H_2S, compared with the gas sensors from pure ZnO nanowires [16]. Zhanying Zhang et al. declaimed that ZnO nanosheets could improve the sensing properties because Pd can catalyze the activation of CH_4 molecules [17].

Besides, the structure of the noble metals is another important factor that can affect the sensing properties of MOS materials to some extent. This is because the microstructure of noble metals greatly affects the gas adsorption, desorption, surface reaction, and electron transfer processes. Hence, synthesizing smaller noble metals, which have large specific surface areas and excellent dispersion, can always improve their properties [18,19]. However, there are few reports on MOS gas sensors sensitized by ultra-fine Pd clusters with a smaller size (<2 nm).

In this work, we synthesized ZnO_{1-x} with more defects by a two-step route method, and then modified ultra-fine Pd Cs on the surface. Through the gas-sensing test, we found that Pd Cs-2/ZnO_{1-x} show a good response to low concentration of CH_4, due to excellent sensitization and catalysis of ultrafine Pd Cs.

2. Materials and Methods

All of the chemicals were purchased from Tianjin Kermel Chemical Reagent Co., Ltd., Tianjin, China and used as received without further purification.

2.1. Synthesis of ZnO NFs

We prepared ZnO NFs using a two-step route, as illustrated in Scheme 1. In the first hydrothermal step, 0.54 g $Zn(CH_3COO)_2 \cdot 2H_2O$ and 1.50 g $Na_3C_6H_5O_7 \cdot 2H_2O$ were dissolved into 30 mL distilled water, and after that 1.20 mL NaOH aqueous solution (0.38 mol/L) was added under vigorous stirring drop by drop. Then, the mixed solution was sealed in an X Teflon-lined stainless-steel autoclave (50 mL) and kept heating at 160 °C for 20 h. Then the material was cooled down to room temperature (RT) in a natural way. After several times of centrifugation, washed with distilled water and ethanol several times, the product was collected then dried at 70 °C for 12 h. As a result, we obtained the Zn-precursor. In the next step, the Zn-precursor was put into a horizontal tube furnace and heated at 500 °C in air for 2 h; finally, we got the ZnO NFs sample.

2.2. Synthesis of ZnO_{1-x} NFs

In a reducing atmosphere (1 bar, 5% H_2, 95% AR), we put a 100.0 mg ZnO sample into a tube furnace, heated at 500 °C for 1 h. Then after cooling down to RT, the dark brown powder ZnO_{1-x} was collected.
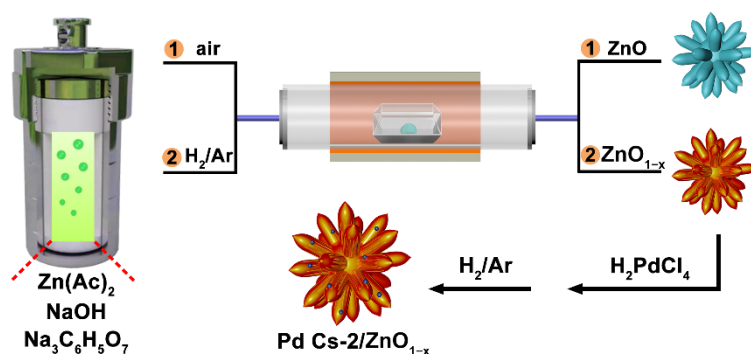
Scheme 1. Illustration of the synthesis of all gas-sensing materials (ZnO, ZnO_{1-x}, Pd Cs-1/ZnO_{1-x}, Pd Cs-2/ZnO_{1-x}, Pd Cs-3/ZnO_{1-x}).

2.3. Synthesis of Pd Cs/ZnO_{1-x}

An amount of 50.0 mg of ZnO_{1-x} NFs were dispersed into a 5.0 mL H_2PdCl_4 solution (1.0 mg/mL) and treated with ultrasound for 90 min. After several centrifugations, washing by distilled water and ethanol, and dried at 60 °C for 8 h, we collected the product. The product was put into the reduced atmosphere (1 bar, 5% H_2, 95% AR). Then the Pd Cs/ZnO_{1-x} was obtained by heating at 200 °C for 1 h; we kept the heating rate at 5 °C/min. In this step, the concentration of H_2PdCl_4 solution was 0.8, 1.0, and 1.2 mg/mL, respectively. Therefore, in these three different Pd Cs/ZnO_{1-x} samples, the mass fraction of Pd Cs is 3.0%, 5.0% and 8.0 wt%, and they are named as Pd Cs-1/ZnO_{1-x}, Pd Cs-2/ ZnO_{1-x}, and Pd Cs-3/ZnO_{1-x}, respectively.

2.4. Characterizations

We used a Rigaku D/max2500 apparatus by using Cu Kα1 radiation (40 mA, 40 kV, 6° min^{-1} from 10 to 80°, Rigaku, Tokyo, Japan) to record the powder X-ray diffraction patterns (PXRD), Field emission scanning electron microscopy (FESEM) images and energy-dispersive X-ray (EDX) mapping were collected on a Hitachi S-4800 SEM (Hitachi, Tokyo, Japan), equipped with an energy-dispersive X-ray (EDX) spectroscope at 5 kV. Samples for SEM imaging were deposited on a conductive adhesive before the test. Transmission Electron Microscope (TEM) and High-resolution Transmission Electron Microscope and (HRTEM) images were recorded on a JEM-2010F electron microscope (JEOL, Tokyo, Japan), operating at 200 kV. X-ray photoelectron spectroscopy (XPS) studies were carried out on a WSCALAB 250Xi (Thermofisher Scientific, Waltham, MA, USA) using an Al Kα monochromated (150 W, 20 eV pass energy, 500 μm spot size). The C1s signal at 284.6 eV was used to calibrate the binding energy scale.

### 2.5. Fabrication and Performance Testing of Gas Sensors

The sensing nanomaterials (ZnO, ZnO_{1-x}, Pd Cs-1/ZnO_{1-x}, Pd Cs-2/ZnO_{1-x}, and Pd Cs-3/ZnO_{1-x}) were grounded with terpineol to form a paste and coated onto the ceramic tubes' surface which was printed with Au electrodes and Pt wires in advance. To remove the adhesive, it was kept sintering at 300 °C for 3 h, then a Ni–Cr alloy coil was inserted into the tube; it was used as a heater to control the operating temperature. The illustration of sensor structure is shown in Scheme 2a. We aged the as-fabricated sensors at 290 °C for 7 days; the aim was to enhance their stability. We used a WS-30A tester (Hanwei Electronics Co. Ltd., Zhengzhou, China) to evaluate the performance of MOS gas sensors. The test circuit illustration is shown in the Scheme 2b. The response of the sensors was R_a/R_g; the R_a and R_g is the resistance of the sensor in the air and in the test gas, respectively. The response and recovery time is counted as the time taken by the sensors output to achieve 90% of the total resistance change after injecting or releasing the test gas. The data are collected at 40% relative humidity (RH) and 25 °C (room temperature). Then, we tested the

effect of RH on the gas-sensing properties of the sensor, and we explored the impact of RH from 40% to 90% on gas sensing. The calculation formula is as follows:

$$V_{sensor} = 5 - V_{out} \qquad (1)$$

$$R_{sensor} = \frac{V_{sensor}}{V_{out}} \times R_L \qquad (2)$$

$$\text{Response} : S = \frac{R_a}{R_g} \ (reducing \ gas) \qquad (3)$$
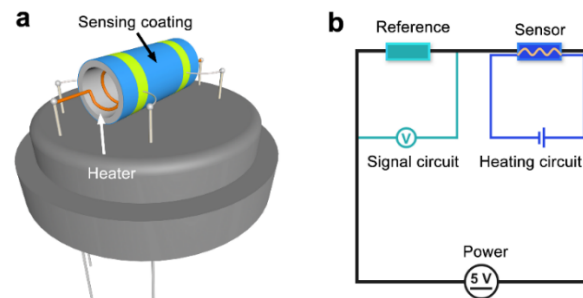
Scheme 2. The illustration of (**a**) basic sensor structure, and (**b**) test circuit.

We repeat all experiments independently for three times.

3. Results

3.1. Characterizations and Analysis

The crystal phase and purity of the ZnO, ZnO_{1-x}, and Pd Cs-1~3/ZnO_{1-x} samples were characterized by XRD. As we can see from Figure 1, the peaks at 31.8°, 34.4°, 36.3°, 47.5°, 56.6°, 62.9°, 66.4°, 68.0°, and 69.1°can be indexed to the (100), (002), (101), (102), (110), (103), (200), (112), and (201) planes of a ZnO crystal given by the standard data files (JCPDS file no. 36-1451), repectively, and we did not find any peaks of other impurities, indicating the high purity of the ZnO NFs sample [20,21]. At the same time, we could not find an obvious change in the intensity of the peaks compared with the pristine ZnO. Besides the ZnO peaks, the peaks of the hexagonal Pd (JCPDS no. 65–3411) are not observed due to extremely small doses and ultra-thin size of Pd Cs, the inspection depth of the instrument, as well as the relative much higher intensity of the ZnO NFs. However, we can prove the existence of Pd Cs exactly in the later experiments (data of TEM images, HRTEM images, XPS, and EDX).
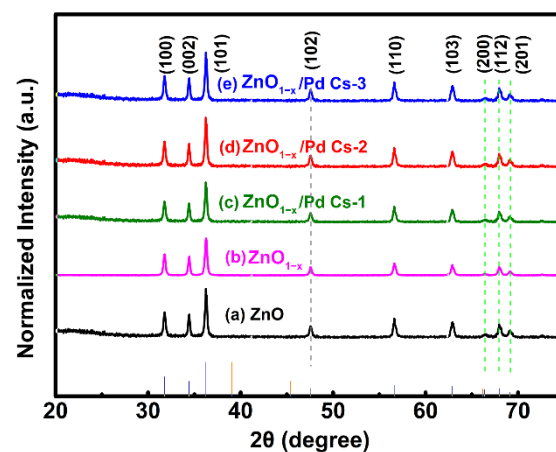

Figure 1. XRD patterns of several nanomaterials ((**a**) ZnO, (**b**) ZnO_{1-x}, (**c**) Pd Cs-1/ ZnO_{1-x}, (**d**) Pd Cs-2/ZnO_{1-x}, (**e**) Pd Cs-3/ZnO_{1-x}, respectively).

The crystal type of ZnO here is hexagonal with the point group P63mc(186), and the parameters of the crystal cell are (a, b, c) = (3.24982, 3.24982, 5.20661) and (α, β, γ) = (90°, 90°, 120°). The lattice distances can be calculated by Bragg equation d = nλ/2sinθ (λ = 0.15406 nm), shown in Table 1, and the grain size can be obtained from the Debye–Scherrer formula D = Kγ/Bcosθ (K = 0.89). Here we used Jade software to grab the information of full width at half maxima, and then calculated the grain sizes of each crystal plane, which are listed in Table 1. The grain sizes distribute from 4.65 to 5.39 nm, and the strongest signal yield crystal plane is (101) with 4.95 nm grain size.

Table 1. Details of ZnO XRD characterization information.

| 2θ	(hkl)	d (Å)	I (f)	Grain Size (nm)
31.77	(100)	2.84	51.7	5.05
34.32	(002)	2.63	42.5	5.22
36.21	(101)	2.50	100	4.95
47.23	(102)	1.93	25.1	5.16
56.30	(110)	1.64	39.2	4.65
62.22	(103)	1.49	41.2	5.39
66.38	(200)	1.42	6.9	4.84
67.36	(112)	1.39	32	5.20
68.62	(201)	1.37	13.8	5.33

FESEM and TEM were applied to characterize the morphologies and microstructures of ZnO, ZnO_{1-x}, and Pd Cs-1~3/ZnO_{1-x}. Firstly, Figure 2a,b exhibit the images of ZnO samples with different magnifications. We can see that ZnO is composed of many flowers with the size around 1 μm. Figure 2b reveals that these NFs are assembled by numerous nanorods with the average length of ~100 nm. We can see the TEM images of the ZnO NFs in Figure 2c. Similar to the above SEM images, these NFs are assembled from many nanorods with diameters of less than 100 nm.
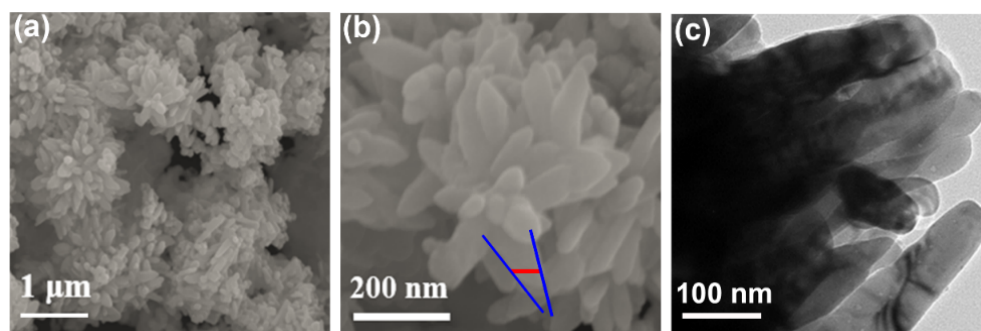
**Figure 2.** SEM (**a**,**b**), and TEM (**c**) images of ZnO NFs.

Figure 3 shows the SEM and TEM images of ZnO_{1-x}. It is found that the morphologies of ZnO_{1-x} NFs have deteriorated a little compared with the ZnO NFs. Figure 3a reveals the building block of ZnO_{1-x} NFs is nanorods with a diameter of ~100 nm. However, when we observe carefully, we can find part of the structure collapse of NFs (Figure 3b), but it is favorable for creating more defects at the same time. The suggestion can be proved by the XPS data in Figure 3. As a result, it can optimize the sensing performances of the ZnO_{1-x} NFs. We can see the fast Fourier transform (FFT) in the insert; the data is in good agreement with the XRD (Figure 1).
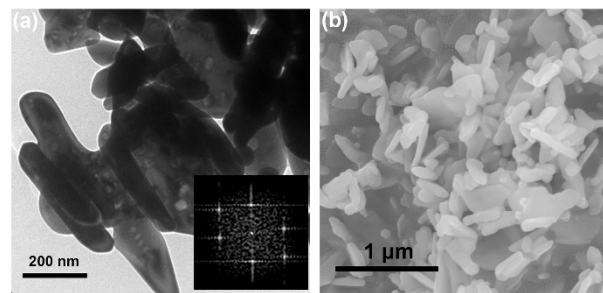
Figure 3. (**a**) TEM images of ZnO_{1-x} and (**b**) SEM images of ZnO_{1-x} (insert: FFT of ZnO_{1-x}).

Figure 4 displays the morphology and microstructure of our Pd Cs-2/ZnO_{1-x}. We can see from Figure 4a,b that Pd Cs are evenly dispersed on the surface of ZnO_{1-x} without aggregation. In addition, the diameter of Pd Cs is just about 1~2 nm, which is significant to enhance its gas-sensing performance by a quantum size effect. In addition, the interplanar spacing information of ZnO_{1-x} and Pd Cs can be seen from Figure 4c, respectively. The measured d spacing (0.260 nm) between the adjacent lattice planes is corresponded to the distance of ZnO (002) crystal planes [22–24]. Another d value of about 0.225 nm can be attributed to (111) planes of Pd Cs [25,26].
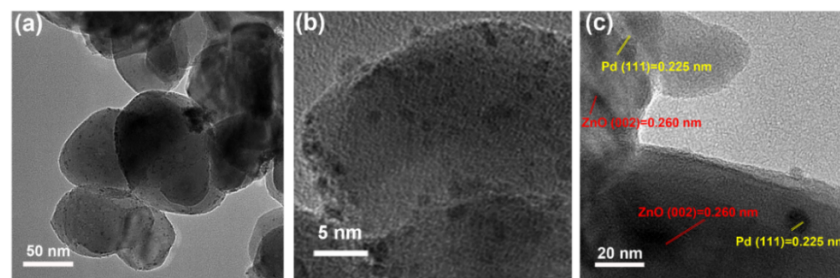

Figure 4. (**a**) TEM, (**b**,**c**) HRTEM images of Pd Cs-2/ZnO_{1-x}.

After that, we can get the information of the EDX elemental mapping data of Pd Cs-2/ZnO_{1-x} to show the distribution of the elements. From Figure 5, it can be seen that this sample is mainly composed of the Zn, O, and Pd elements, and they are distributed uniformly. We can see from Figure 5b,c that the O and Zn elements distribute evenly, which matches the properties of the ZnO nanomaterial. It is worth noting that Pd Cs are homogeneously distributed around the whole ZnO_{1-x} material and have good dispersion without obvious accumulation and aggregation, which will be beneficial to the gas sensing of the material.
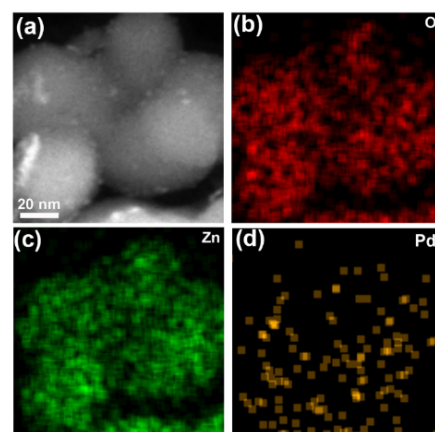

Figure 5. The EDX elemental mapping data of Pd Cs-2/ZnO_{1-x}: (**a**) TEM image, (**b**) O element, (**c**) Zn element, and (**d**) Pd element.

Next, Figure 6 shows the TEM images of these three Pd Cs 1~3/ZnO_{1-x} nanomaterials. From the figure, we know that with the increase in precursor H_2PdCl_4, the content of Pd Cs in the synthesized nanomaterials increases gradually, and we can see from Figure 6b that they are uniformly distributed on the surface of ZnO_{1-x}. However, with the further increase in it, the Pd Cs aggregate on the surface of ZnO_{1-x}, resulting in a negative effect on the gas-sensing performances of the synthesized nanomaterials, as shown in Figure 6c.
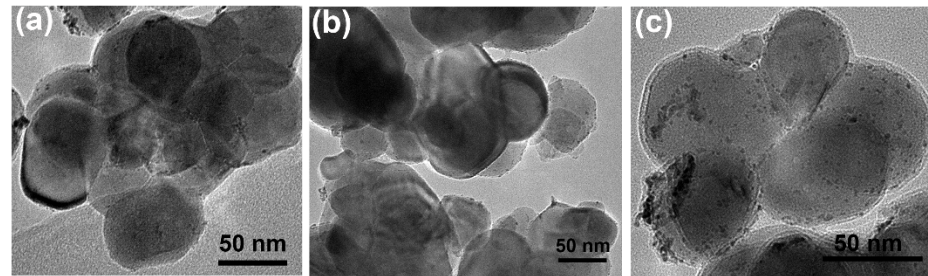

Figure 6. TEM images of three nanomaterials ((**a**) Pd Cs-1/ZnO_{1-x}, (**b**) Pd Cs-2/ZnO_{1-x}, and (**c**) Pd Cs-3/ZnO_{1-x}, respectively).

Next, we tested these gas-sensing materials' surface chemical compositions using X-ray photoelectron spectroscopy (XPS) and show them in Figure 7a. We can clearly see the Zn, O, and Pd peaks, with no other peaks (except C) appearing. After that we analyzed and discussed the valence states of them. Figure 7b exhibits the Zn 2p spectra of ZnO, ZnO_{1-x}, and Pd Cs-2/ZnO_{1-x}. Figure 7b shows that the peaks of Zn $2p_{3/2}$ of ZnO and ZnO_{1-x} is about 1021.3 eV, and the peaks of Zn $2p_{1/2}$ of ZnO and ZnO_{1-x} are 1044.0 eV, showing that Zn element is in the formal Zn^{2+} valence state. At the same time, we know that the two peaks of Pd Cs-2/ZnO_{1-x} shift to a low binding energy of about 1020.9 eV and 1044.0 eV for Zn $2p_{3/2}$ and Zn $2p_{1/2}$. This shift is mainly due to the interaction between ZnO_{1-x} and Pd Cs, which can change ZnO_{1-x}'s surface electronic structure and as a result, enhance its sensing performance. For Pd element, as we can see from Figure 7c, the peaks at 334.6 and 340.0 eV are Pd $3d_{5/2}$ and Pd $3d_{3/2}$, respectively, which only belongs to Pd^0 state [27–29].
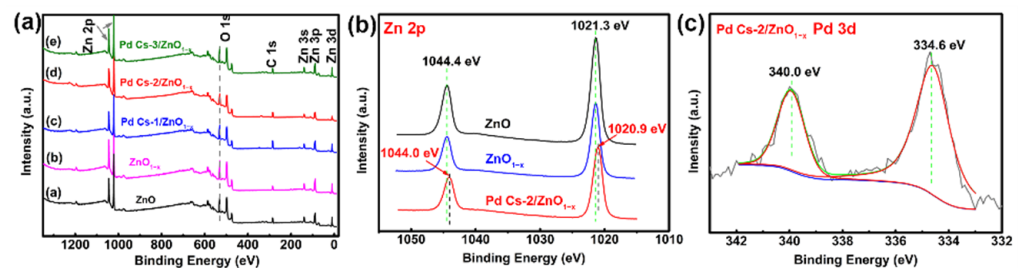
Figure 7. (**a**) XPS survey scan for five gas-sensing materials, (**b**) Zn 2p spectrum of ZnO, ZnO_{1-x} and Pd Cs-2/ZnO_{1-x}, and (**c**) Pd 3d spectrum of Pd Cs-2/ZnO_{1-x}, respectively.

The O 1s spectra in Figure 8 reveal the states of surface O of three gas-sensing materials. O_I and O_{II} are two states of O (O_I is lattice oxygen; O_{II} is oxygen defects). For ZnO as well as ZnO_{1-x}, the peaks at 530.1 eV and 531.8 eV are O_I and O_{II}, respectively. We can find that the OII proportion in ZnO and ZnO_{1-x} is 31.60% and 38.82%, respectively (shown in Table 1), proving there is more oxygen defects existing on the surface of these materials that will influence their sensing materials. As such, the O 1s peaks of Pd Cs-2/ZnO_{1-x} shift to low binding energy at 529.9 eV and 531.5 eV for the reason we discussed earlier. Table 2 gives the specific proportion of O 1s peaks among ZnO, ZnO_{1-x} and Pd Cs-2/ZnO_{1-x} [30].
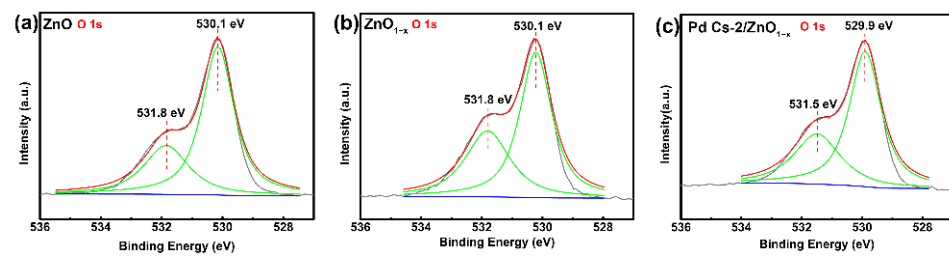
Figure 8. O 1s spectra of (**a**) ZnO, (**b**) ZnO_{1-x} and (**c**) Pd Cs-2/ZnO_{1-x}.

Table 2. Corresponding Percentage of O 1s Peaks among ZnO, ZnO_{1-x} and Pd Cs-2/ZnO_{1-x}, respectively (%).

Type of Oxygen	ZnO	ZnO_{1-x}	Pd Cs-2/ZnO_{1-x}
O_I (lattice oxygen)	68.40	61.18	62.15
O_{II} (oxygen defects)	31.60	38.82	37.85

Further, we performed photoluminescence (PL) spectra on the samples ZnO, ZnO_{1-x}, and Pd Cs-2/ZnO_{1-x}, as we can see in Figure 9. From the original curves, we know that the whole PL spectrum in the range 380~500 nm can be Gaussian deconvoluted into different parts; these parts represent different defects. Particularly, Zn_i and V_O are electron donors in different materials, and the donors have a huge impact on its sensitivity. Firstly, we nearly could not find the signals of Zn_i and V_O in ZnO because of a few contents as well as the detection depth of the instrument. However, we found that after calcination in a reduced atmosphere in the tubular furnace, oxygen vacancy defects in ZnO_{1-x} are more than that of ZnO (the purple line and the blue line in Figure 9). Furthermore, after another calcination step in the reduced atmosphere, there are many more oxygen defects generated in Pd Cs-2/ZnO_{1-x}. In addition, we calculated the ratio of V_O/Zn_i in different samples; the data of ZnO_{1-x} and Pd Cs-2/ZnO_{1-x} are 3.54 and 12.17, respectively, proving more oxygen vacancies existed in Pd Cs-2/ZnO_{1-x} [31].
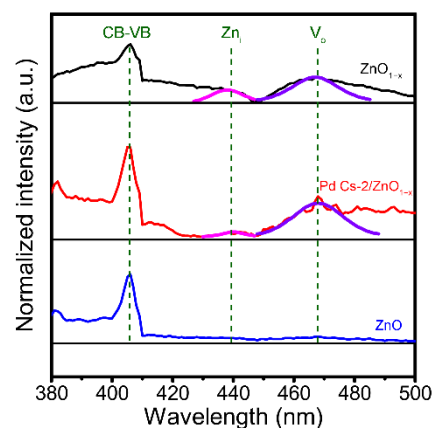
Figure 9. Photoluminescence spectroscopy of different products (ZnO, ZnO_{1-x} and Pd Cs-2/ZnO_{1-x}, respectively).

3.2. Gas-Sensing Properties

Firstly, the operating temperature could influence the gas-sensing process to a large extent. Therefore, it is necessary for us to determine their optimum working temperature [32]. Because of the high symmetry and stability of CH_4 molecules, a relative high working temperature for CH_4 sensing is required. Hence, we tested temperature-dependent gas responses from 200 to 300 °C. In this process, we found that the responses to different gases change significantly with working temperature, as shown in Figure 10. The detected

gases include methane, methanol, acetone, formaldehyde, benzene, and ammonia. When the operating temperature increases, the responses of all the sensors increase gradually, then reaching a maximum at a specific temperature. For ZnO and ZnO_{1-x} gas sensors, the maximum gas response appears at 280 °C (2.5 and 3.0 to 50 ppm CH_4, respectively). The response of Pd Cs-1~3/ZnO_{1-x} gas sensors reach the highest gas response at 260 °C, indicating Pd Cs have catalytic activity to CH_4 oxidization, thus decreasing its reactive and sensing temperature. Their responses to 50 ppm CH_4 are 5.0, 4.6, and 4.3 for Pd Cs-2/ZnO_{1-x}, Pd Cs-3/ZnO_{1-x}, and Pd Cs-1/ZnO_{1-x}, respectively. After that, the responses of all the gas-sensing materials decrease slowly. So, we selected 260 °C as the optimal working temperature to further study the gas-sensing performance of Pd Cs-2/ZnO_{1-x} gas sensors.
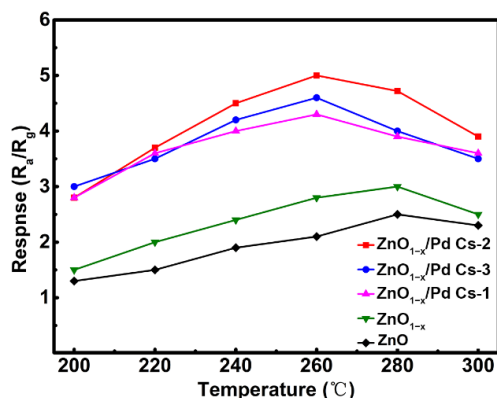

Figure 10. Response of all the sensors to CH_4 at different operating temperatures (to 50 ppm, from 200 to 300 °C), 40% RH.

To study the gas selectivity of the sensors [33], we also tested their gas responses to the other 50 ppm gases as we mentioned earlier at 260 °C at the same time. As we can see from Figure 11a, the sensor Pd Cs-2/ZnO_{1-x} has better gas selectivity than any other counterparts. The responses to 50 ppm methane, methanol, acetone, formaldehyde, benzene, and ammonia is 5.0, 2.1, 1.5, 1.7, 1.3, and 1.4, respectively, indicating a good selectivity to methane. Therefore, the decoration of ZnO_{1-x} with certain content Pd Cs not only improved their gas responses, but also optimized their gas selectivity. Figure 11b shows the illustration of relative selectivity of these five different sensors.
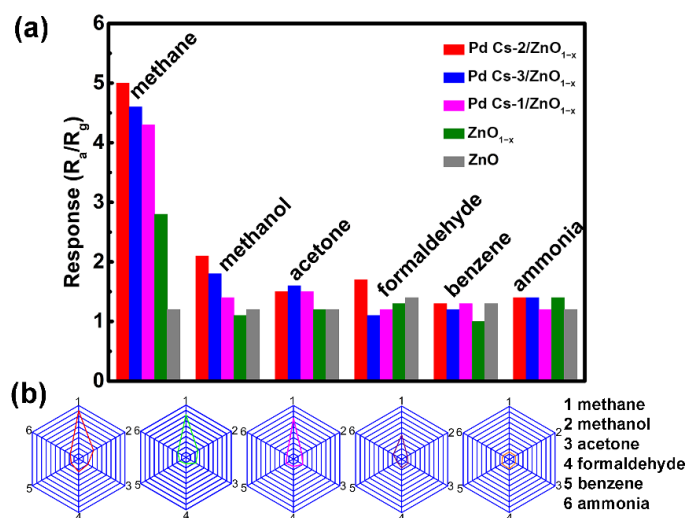

Figure 11. (**a**) Sensors' selectivity: the representative responses of five different gas-sensing materials to different VOCs (50 ppm) at 260 °C, 40% RH. (**b**) Illustration of relative selectivity of five different sensors (Pd Cs-2/ZnO_{1-x}, Pd Cs-3/ZnO_{1-x}, Pd Cs-1/ZnO_{1-x}, ZnO_{1-x}, and ZnO, respectively).

It is meaningful to determine the dynamic sensors' response [34]. The response and recovery curve of Pd Cs-2/ZnO$_{1-x}$ gas sensor to CH$_4$ at 260 °C is shown in Figure 12a. We know that the response and recovery times of 50 ppm CH$_4$ are 16.2 s and 13.8 s, respectively. In addition, we can see that with the concentration changes, the response increases from 2.3 (10 ppm CH$_4$) to 5.0 (50 ppm CH$_4$) gradually, and it conforms to an excellent linear relationship (the R^2 is 0.963), as we can see from Figure 12b.
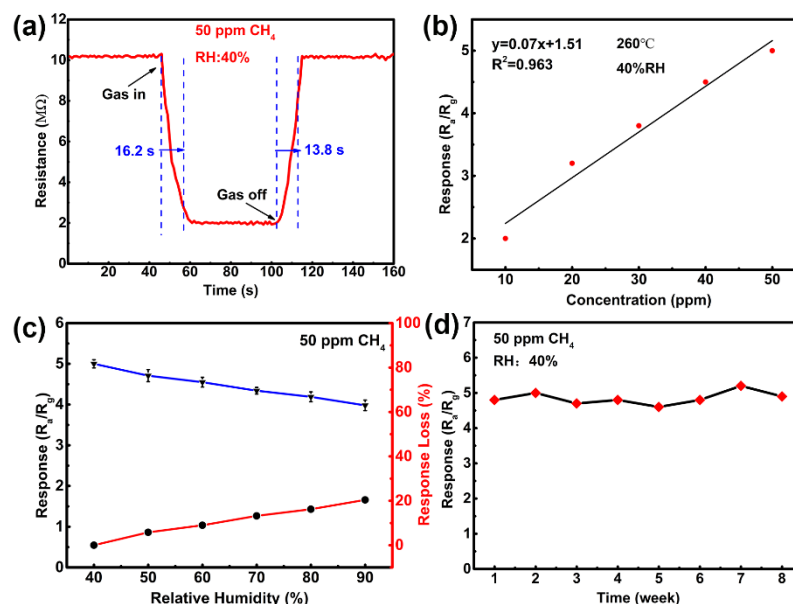
Figure 12. (**a**). Response and recovery curve of Pd Cs-2/ZnO$_{1-x}$ sensor (50 ppm CH$_4$ at 260 °C, 40% RH); (**b**) The responses to different concentrations of CH$_4$(260 °C, 40% RH, 10~50 ppm) as well as their fitting curve; (**c**) The relationship between response and response loss ratio, as well as RH (50 ppm CH$_4$ at 260 °C); and (**d**) The stability of Pd Cs-2/ZnO$_{1-x}$ gas sensor to 50 ppm CH$_4$ within 8 weeks, 40% RH.

We should not ignore that relative humidity (RH) has an impact on their gas-sensing performance [35]. Therefore, it is indeed necessary to explore their gas-sensing properties at a high-humidity environment. We can see the sensing performance ranging from 40% to 90% in Figure 12c. When RH varies, the sensors' response to methane decreases conversely, showing that RH truly influences methane detection. When RH was 90%, the response decreased by 20.4% (to 50 ppm CH$_4$ at its optimum temperature). As a result, we should focus on the influence of RH, and do a good job of compensation and protection for the sensor devices. For example, compensating it through the circuit when fabricating devices.

Last, we analyzed the long-term stability of the sensor (260 °C, 40% RH); the results are shown in Figure 12d [36]. We can see from the figure that the responses of the sensor are stable within 8 weeks; the response is fluctuant between 4.7~5.2 for 50 ppm CH$_4$. In a word, the ZnO$_{1-x}$/Pd Cs-2 gas sensor has a great response; good selectivity, response and recovery properties; and a satisfactory long-term sensing property, meaning it is an ideal candidate for detecting low-concentration CH$_4$.

3.3. Mechanism of Gas-Sensing Performance

We know that the sensing mechanism of MOS mainly depends on its resistance to the surface change where the surface states and adsorbing capacity of oxygen play important roles, for example, the redox reaction of the detected gas on the MOS surface with the chemisorbed oxygen species, such as O$_2^-$, O$^-$ and O^{2-} [37,38].

Firstly, the sensing material is Pd Cs/ZnO$_{1-x}$ with many more oxygen defects than ZnO NFs, so it has many more adsorption sites and a low transport barrier. As a result, we can see that the R$_a$ of ZnO$_{1-x}$ is much less than that of ZnO, proving there are many more

carriers in ZnO_{1-x} [39,40]. Secondly, the decoration of Pd Cs is essential in optimizing its performance. We all know that the high catalytic ability of Pd Cs can improve the gas-sensing properties, including increase in gas response and decrease in the working temperature [41,42]. In addition, the electronic sensitization of Pd Cs is clear for improving the gas response and selectivity to CH_4. Due to different functions of Pd (5.6 eV) and ZnO (5.2 eV), the electron flow to Pd Cs from ZnO, lead to an increase in the electron depletion layer thickness at the interface between ZnO and Pd, as we can see in Figure 13. The R_a of Pd Cs-2/ZnO_{1-x} is about 10.52 MΩ, which is much higher than that of ZnO and ZnO_{1-x} (4.3 and 2.2 MΩ, respectively). In general, for an n-type MOS sensor, a relative high R_a is good to achieve a higher response; the reason is that the gas response was R_a/R_g. The more Pd Cs that exist on the surface, the more the R_a of the material increases.
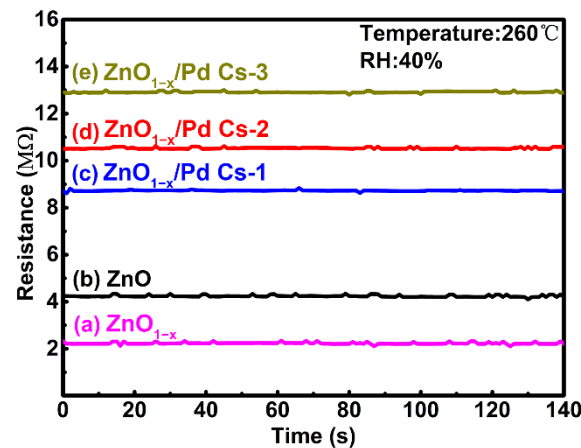

Figure 13. Base resistance in the air of the obtained sensors at 260 °C, 40% RH.

Finally, the small sizes of Pd Cs cannot be ignored to improve the performance of our gas-sensing materials [43,44]. As the size of Pd Cs decreases to less 2 nm, the number of exposed surface atoms increases significantly. At the same time, it is accompanied by the changes of surface atomic structure, electronic structure, and surface defects; almost every Pd atom of Pd Cs is participant in the gas-sensing process, resulting in the utilization ratio being much higher. Consequently, there will be more electrons moving to Pd Cs, resulting in a thicker electronics depletion layer of ZnO_{1-x}. In addition, because of the quantum size effect, the surface activity of Pd Cs increases rapidly with a decrease in its size, thus leading to further performance improvement. Figure 14 is the schematic diagram of the gas-sensing mechanism of this process [45].
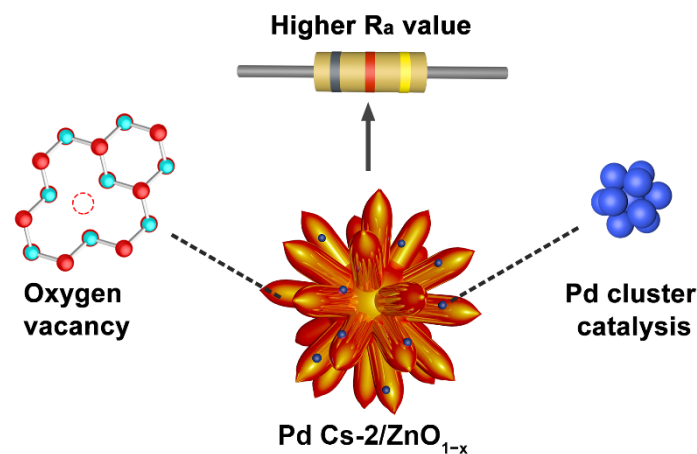

Figure 14. Illustration of the gas-sensing mechanism.

4. Conclusions

In summary, ZnO_{1-x} NFs with more oxygen vacancies were synthesized by treatment of a H_2 atmosphere and decorated with ultra-thin Pd clusters to prepare Pd Cs-2/ZnO_{1-x} gas-sensing materials. It has been found that Pd Cs-2/ZnO_{1-x} gas sensors show enhanced gas-sensing properties to low-concentration CH_4 at 260 °C, to 50 ppm CH_4, and the response is 5.0; the time of response and recovery are just 16.2 s and 13.8 s, respectively. These enhanced sensing properties are due to catalytic, electronic sensitization and the quantum size effect of ultra-thin Pd clusters, defect engineering, convenient gas diffusion, and the high specific surface area of ZnO nanoflowers as well as their synergistic effect. This work has excellent potential in the detection of low concentration of CH_4 for cancer diagnosis.

Author Contributions: Methodology, Y.C.; software, Y.C.; validation, Y.C., W.Z. and N.L.; formal analysis, W.W.; resources, W.W.; writing—original draft preparation, W.Z.; writing—review and editing, J.X.; visualization, W.Z.; project administration, J.X.; funding acquisition, J.X. All authors have read and agreed to the published version of the manuscript.

Institutional Review Board Statement: Not applicable.

Informed Consent Statement: Not applicable.

Data Availability Statement: Not applicable.

Conflicts of Interest: The authors declare no conflict of interest.

References

1. Ghosh, S.; Roy Chaudhuri, C.; Bhattacharya, R.; Saha, H.; Mukherjee, N. Palladium–Silver-Activated ZnO Surface: Highly Selective Methane Sensor at Reasonably Low Operating Temperature. *ACS Appl. Mater. Interfaces* **2014**, *6*, 3879–3887. [CrossRef] [PubMed]
2. Dong, L.; Li, C.; Sanchez, N.P.; Gluszek, A.K.; Tittel, F.K. Compact CH4 sensor system based on a continuous-wave, low power consumption, room temperature interband cascade laser. *Appl. Phys. Lett.* **2016**, *108*, 011106. [CrossRef]
3. Zhang, W.; Yuan, T.; Wang, X.; Cheng, Z.; Xu, J. Coal mine gases sensors with dual selectivity at variable temperatures based on a W18O49 ultra-fine nanowires/Pd@Au bimetallic nanoparticles composite. *Sens. Actuators B Chem.* **2021**, *354*, 131004. [CrossRef]
4. Haridas, D.; Gupta, V. Enhanced response characteristics of SnO2 thin film based sensors loaded with Pd clusters for methane detection. *Sensors Actuators B: Chem.* **2012**, *166–167*, 156–164. [CrossRef]
5. Yuan, T.; Li, Z.; Zhang, W.; Xue, Z.; Wang, X.; Ma, Z.; Fan, Y.; Xu, J.; Yuen, W. Highly sensitive ethanol gas sensor based on ultrathin nanosheets as-sembled Bi2WO6 with composite phase. *Sci. Bull.* **2019**, *64*, 595–602. [CrossRef]
6. Li, G.; Wang, X.; Yan, L.; Wang, Y.; Zhang, Z.; Xu, J. PdPt Bimetal-Functionalized SnO_2 Nanosheets: Controllable Synthesis and its Dual Selectivity for Detection of Carbon Monoxide and Methane. *ACS Appl. Mater. Interfaces* **2019**, *11*, 26116–26126. [CrossRef]
7. Rianjanu, A.; Fauzi, F.; Triyana, K.; Wasisto, H.S. Electrospun Nanofibers for Quartz Crystal Microbalance Gas Sensors: A Review. *ACS Appl. Nanomater.* **2021**, *4*, 9957–9975. [CrossRef]
8. Rezki, M.; Septiani, N.L.W.; Iqbal, M.; Adhika, D.R.; Wenten, I.G.; Yuliarto, B. Review—Recent Advance in Multi-Metallic Metal Organic Frameworks (MM-MOFs) and Their Derivatives for Electrochemical Biosensor Application. *J. Electrochem. Soc.* **2022**, *169*, 017504. [CrossRef]
9. Tian, W.; Liu, X.; Yu, W. Research Progress of Gas Sensor Based on Graphene and Its Derivatives: A Review. *Appl. Sci.* **2018**, *8*, 1118. [CrossRef]
10. Pra, C.; Cra, B.; Is, A.; Jgp, A.; Hpan, A.; Mndsc, C. Molecularly imprinted polymer-based electrochemical sensors for environmental analysis—ScienceDirect. *Biosens. Bioelectron.* **2010**, *172*, 112719–112727.
11. Zhou, Q.; Zeng, W.; Chen, W.; Xu, L.; Kumar, R.; Umar, A. High sensitive and low-concentration sulfur dioxide (SO2) gas sensor application of heterostructure NiO-ZnO nanodisks. *Sens. Actuators* **2019**, *298*, 126870. [CrossRef]
12. Xu, F.; Zhou, C.; Ho, H.P. A rule for operation temperature selection of a conductometric VOC gas sensor based on ZnO nan-otetrapods. *J. Alloy. Compd.* **2020**, *858*, 158294. [CrossRef]
13. Suematsu, K.; Watanabe, K.; Tou, A.; Sun, Y.; Shimanoe, K. Ultraselective Toluene-Gas Sensor: Nanosized Gold Loaded on Zinc Oxide Nanoparticles. *Anal. Chem.* **2018**, *90*, 1959–1966. [CrossRef]
14. Qin, Y.; Liu, D.; Zhang, T.; Cui, Z. Ultrasensitive Silicon Nanowire Sensor Developed by a Special Ag Modification Process for Rapid NH_3 Detection. *ACS Appl. Mater. Interfaces* **2017**, *9*, 28766–28773. [CrossRef]
15. Kim, J.C.; Jun, H.K.; Huh, J.; Lee, D.D. Tin oxide-based methane gas sensor promoted by alumina-supported Pd catalyst. *Sens. Actuators B Chem.* **1997**, *45*, 271–277. [CrossRef]

16. Zhang, Y.; Xiang, Q.; Xu, J.; Xu, P.; Pan, Q.; Li, F. Self-assemblies of Pd nanoparticles on the surfaces of single crystal ZnO nan-owires for chemical sensors with enhanced performances. *J. Mater. Chem.* **2009**, *19*, 4701–4706. [CrossRef]

17. Wang, Y.; Meng, X.; Yao, M.; Sun, G.; Zhang, Z. Enhanced CH4 sensing properties of Pd modified ZnO nanosheets. *Ceram. Int.* **2019**, *45*, 13150–13157. [CrossRef]

18. He, H.; Xue, Y.-Q.; Wang, S.-Q.; Zhu, Q.-Q.; Chen, J.; Li, C.-P.; Du, M. A Double-Walled Bimetal–Organic Framework for Antibiotics Sensing and Size-Selective Catalysis. *Inorg. Chem.* **2018**, *57*, 15062–15068. [CrossRef]

19. Su, P.-G.; Yu, J.-H. Enhanced NO2 gas-sensing properties of Au-Ag bimetal decorated MWCNTs/WO3 composite sensor under UV-LED irradiation. *Sens. Actuators A Phys.* **2019**, *303*, 111718. [CrossRef]

20. Xing, L.; Ma, C.; Chen, Z.-H.; Chen, Y.-J.; Xue, X.-Y. High gas sensing performance of one-step-synthesized Pd–ZnO nanoflowers due to surface reactions and modifications. *Nanotechnology* **2011**, *22*, 215501. [CrossRef]

21. Singh, B.V.; Sapana, R.; Saravanan, R.; Kumari, K.; Raliya, R.; Biswas, P.; Kumar, M. Improved Sensitivity with Low Limit of Detection of a Hydrogen Gas Sensor Based on rGO-Loaded Ni-Doped ZnO Nanostructures. *ACS Appl. Mater. Interfaces* **2018**, *10*, 11116–11124.

22. Kim, H.; Jin, C.; Park, S.; Lee, C. Enhanced H2S gas sensing properties of multiple-networked Pd-doped SnO2-core/ZnO-shell nanorod sensors. *Mater. Res. Bull.* **2012**, *47*, 2708–2712. [CrossRef]

23. Ning, Y.; Fielding, L.A.; Nutter, J.; Kulak, A.N.; Meldrum, F.C.; Armes, S.P. Spatially Controlled Occlusion of Polymer-Stabilized Gold Nanoparticles within ZnO. *Angew. Chem.* **2019**, *131*, 4346–4351. [CrossRef]

24. Zabilskiy, M.; Sushkevich, V.L.; Newton, M.A.; Krumeich, F.; Nachtegaal, M.; Bokhoven, J.A.V. Mechanistic study of carbon dioxide hydrogenation over Pd/ZnO-based catalysts: The role of palladium-zinc alloy in selective methanol synthesis. *Angew. Chem.* **2021**, *133*, 17190–17196. [CrossRef]

25. Shon, G.Y.S. Controlling Surface Ligand Density and Core Size of Alkanethiolate-Capped Pd Nanoparticles and Their Effects on Catalysis. *Langmuir* **2012**, *28*, 14502–14508.

26. Zhou, H.; Yang, X.; Li, L.; Liu, X.; Huang, Y.; Pan, X.; Wang, A.; Li, J.; Zhang, T. PdZn Intermetallic Nanostructure with Pd–Zn–Pd Ensembles for Highly Active and Chemoselective Semi-Hydrogenation of Acetylene. *ACS Catal.* **2016**, *6*, 1054–1061. [CrossRef]

27. Chang, Y.; Xu, J.; Zhang, Y.; Ma, S.; Xin, L.; Zhu, L.; Xu, C. Optical Properties and Photocatalytic Performances of Pd Modified ZnO Samples. *J. Phys. Chem. C* **2009**, *113*, 18761–18767. [CrossRef]

28. Platonov, V.; Rumyantseva, M.; Khmelevsky, N.; Gaskov, A. Electrospun ZnO/Pd Nanofibers: CO Sensing and Humidity Effect. *Sensors* **2020**, *20*, 7333. [CrossRef]

29. Zhu, Q.; Xie, C. Comparative study of ZnO nanorod array and nanoparticle film in photoelectric response and charge storage. *J. Alloys Compd.* **2014**, *585*, 267–276. [CrossRef]

30. Geng, Z.; Kong, X.; Chen, W.; Su, H.; Liu, Y.; Cai, F.; Wang, G.; Zeng, J. Oxygen Vacancies in ZnO Nanosheets Enhance CO$_2$ Electrochemical Reduction to CO. *Angew. Chem.* **2018**, *130*, 6162–6167. [CrossRef]

31. Xue, Z.; Cheng, Z.; Xu, J.; Xiang, Q.; Wang, X.; Xu, J. Controllable Evolution of Dual Defect Zn$_i$ and V$_O$ Associate-Rich ZnO Nanodishes with (0001) Exposed Facet and Its Multiple Sensitization Effect for Ethanol Detection. *ACS Appl. Mater. Interfaces* **2017**, *9*, 41559–41567. [CrossRef] [PubMed]

32. Zhang, W.; Fan, Y.; Yuan, T.; Lu, B.; Liu, Y.; Li, Z.; Li, G.; Cheng, Z.; Xu, J. Ultrafine Tungsten Oxide Nanowires: Synthesis and Highly Selective Acetone Sensing and Mechanism Analysis. *ACS Appl. Mater. Interfaces* **2019**, *12*, 3755–3763. [CrossRef] [PubMed]

33. Rong, Q.; Xiao, B.; Zeng, J.; Yu, R.; Zi, B.; Zhang, G. Pt Single Atom-Induced Activation Energy and Adsorption En-hancement for an Ultrasensitive ppb-Level Methanol Gas Sensor. *ACS Sens.* **2021**, *7*, 199–206. [CrossRef] [PubMed]

34. Drobek, M.; Kim, J.-H.; Bechelany, M.; Vallicari, C.; Julbe, A.; Kim, S.S. MOF-Based Membrane Encapsulated ZnO Nanowires for Enhanced Gas Sensor Selectivity. *ACS Appl. Mater. Interfaces* **2016**, *8*, 8323–8328. [CrossRef]

35. Kuang, Q.; Lao, C.; Wang, Z.L.; Xie, Z.; Zheng, L. High-Sensitivity Humidity Sensor Based on a Single SnO$_2$ Nanowire. *J. Am. Chem. Soc.* **2007**, *129*, 6070–6071. [CrossRef]

36. Lu, Y.; Jiang, Y.; Gao, X.; Wang, X.; Chen, W. Strongly Coupled Pd Nanotetrahedron/Tungsten Oxide Nanosheet Hybrids with Enhanced Catalytic Activity and Stability as Oxygen Reduction Electrocatalysts. *J. Am. Chem. Soc.* **2014**, *136*, 11687–11697. [CrossRef]

37. Koo, W.-T.; Yu, S.; Choi, S.-J.; Jang, J.-S.; Cheong, J.Y.; Kim, I.-D. Nanoscale PdO Catalyst Functionalized Co$_3$O$_4$ Hollow Nanocages Using MOF Templates for Selective Detection of Acetone Molecules in Exhaled Breath. *ACS Appl. Mater. Interfaces* **2017**, *9*, 8201–8210. [CrossRef]

38. Barsan, N.; Koziej, D.; Weimar, U. Metal oxide-based gas sensor research: How to? *Sens. Actuators B Chem.* **2007**, *121*, 18–35. [CrossRef]

39. Luo, N.; Wang, C.; Zhang, D.; Guo, M.; Wang, X.; Cheng, Z.; Xu, J. Ultralow detection limit MEMS hydrogen sensor based on SnO2 with oxygen vacancies. *Sens. Actuators B Chem.* **2021**, *354*, 130982. [CrossRef]

40. Xu, Y.; Zheng, L.; Yang, C.; Zheng, W.; Liu, X.; Zhang, J. Oxygen Vacancies Enabled Porous SnO$_2$ Thin Films for Highly Sensitive Detection of Triethylamine at Room Temperature. *ACS Appl. Mater. Interfaces* **2020**, *12*, 20704–20713. [CrossRef]

41. Bhardwaj, R.; Selamneni, V.; Thakur, U.N.; Sahatiya, P.; Hazra, A. Detection and discrimination of volatile organic compounds by noble metal nanoparticle functionalized MoS$_2$ coated biodegradable paper sensors. *New J. Chem.* **2020**, *44*, 16613–16625. [CrossRef]

42. Baek, D.-H.; Kim, J. MoS$_2$ gas sensor functionalized by Pd for the detection of hydrogen. *Sens. Actuators B Chem.* **2017**, *250*, 686–691. [CrossRef]

43. Penza, M.; Rossi, R.; Alvisi, M.; Cassano, G.; Signore, M.; Serra, E.; Giorgi, R. Pt- and Pd-nanoclusters functionalized carbon nanotubes networked films for sub-ppm gas sensors. *Sens. Actuators B Chem.* **2008**, *135*, 289–297. [CrossRef]

44. Ayesh, A.I. Linear hydrogen gas sensors based on bimetallic nanoclusters. *J. Alloy. Compd.* **2016**, *689*, 1–5. [CrossRef]

45. Luo, N.; Zhang, B.; Zhang, D.; Xu, J. Enhanced CO sensing properties of Pd modified ZnO porous nanosheets. *Chin. Chem. Lett.* **2020**, *31*, 2033–2036. [CrossRef]